

Design of laser parameters for selectively laser melted maraging steel based on deposited energy density

Asuka Suzuki¹ *, Ryoya Nishida¹, Naoki Takata¹, Makoto Kobashi¹, and Masaki Kato²

¹ Department of Materials Process Engineering, Graduate School of Engineering, Nagoya University, Furo-cho, Chikusa-ku, Nagoya, 464-8603, Japan

² Aichi Center for Industry and Science Technology, 1267-1 Aikai, Yakusa-cho, Toyota 470-0356, Japan

* Corresponding author: Asuka Suzuki

E-mail address: suzuki.asuka@material.nagoya-u.ac.jp

Abstract

In this study, the effect of laser power and scan speed on the relative density, melt pool depth, and Vickers hardness of selectively laser melted (SLM) maraging steel were systematically investigated. The change in these structural parameters and hardness could not be always clarified by the volumetric energy density, which is widely used in the SLM processes. The deposited energy density, wherein the thermal diffusion length is used as a heat-distributed depth, could express the change in these structural parameters and the hardness with one curve. To clarify the effect of the laser parameters, the deposited energy should be used instead of the volumetric energy density. Thus, this study provides a new insight for the selection of the laser condition for SLM-fabricated materials.

Keywords: selective laser melting; maraging steel; energy density; relative density;

1. Introduction

Additive manufacturing (AM) is a promising technique that makes possible the fabrication of complex-shaped metal products [1-4]. One of the most popular AM processes for metals is selective laser melting (SLM) with powder-bed system [2]. In the SLM process, thin-layered powder particles of metals (alloys) are repeatedly bedded and fused by laser irradiation. An interesting feature of the SLM process is the formation of anomalous microstructures. Laser irradiation melts powder particles locally to generate semi-cylindrical melt pools, and the subsequent rapid solidification forms a fine microstructure with anisotropy [5-8].

The SLM process has been applied to various alloy powders [8-11]. For example, maraging steel, which is a high-strength special steel reinforced with intermetallic compounds instead of carbides, is one of the steels used in the SLM process because of its good weldability [11-14]. The maraging steels are widely used as tool steels in the mold and die-making industries [15]. Therefore, it is expected that high-performance molds and dies of maraging steels (e.g., high cooling efficiency molds with complicated water pipe) can be manufactured through the SLM process. In order to achieve such high-performance molds and dies, it is important to understand the microstructure and properties of SLM-fabricated maraging steels. Previous studies have investigated the effects of laser scanning conditions and heat treatments on the mechanical properties of the maraging steel fabricated through the SLM process [13, 16-18]. The results of our previous study revealed the crystallographic features of the martensite structure in the SLM-fabricated maraging steel [19].

In the SLM process, it is important to select the building conditions according to the materials. If the materials are fabricated under inappropriate building conditions, they become porous and do not exhibit good mechanical properties. Many researchers have investigated the effects of the laser parameters on the relative density of SLM-fabricated alloys [20-24]. The following volumetric energy density (E_d) has been widely used to investigate the effects of laser parameters.

$$E_d = \frac{P}{v \cdot S \cdot t}, \quad (1)$$

where P is the laser power, v is the laser-scanning speed, S is the hatch spacing between adjacent laser-scanning tracks, and t is the bedded-power layer thickness. However, it remains unclear whether the volumetric energy density is appropriate to represent the influence of the laser conditions [25].

In this study, the effects of the laser conditions on the relative density, melt pool depth, and microhardness of SLM-fabricated maraging steel were systematically investigated.

In particular, another parameter was used instead of the volumetric energy density.

2. Experimental procedure

In the experiment, maraging steel powder, whose details have been presented in our previous report, was used [19]. The SLM processing was conducted at room temperature using the 3D systems ProX 200 (3D SYSTEMS, Rock Hill, SC, USA) additive-manufacturing system equipped with an Yb-fiber laser. A hexagonal grid laser-scanning pattern was applied [19]. The fabrication parameters used in this research were as follows: the laser spot size was approximately 100 μm , which was determined by the extent of negatively defocusing (convergent nature) [26] from the focal position of the laser; the bedded-powder layer thickness was 30 μm ; the hatch spacing between adjacent laser-scanning tracks was 50 μm ; the rotation angle between the bedded-powder layers was 90°. Fig. 1 shows (a) the appearance of the fabricated samples and (b) the laser conditions applied in this study. 25 cuboidal samples with a size of approximately $15 \times 15 \times 15 \text{ mm}^3$ were fabricated with different laser powers and scan speeds. The numbers near the circles shown in Fig. 1(b) correspond to the numbers of the samples shown in Fig. 1(a). The laser parameters were set such that the conditions with the same volumetric energy density were included. All the conditions falling on the dashed line shown in Fig. 1 (b) had a constant volumetric energy density of approximately $68 \text{ J} \cdot \text{mm}^{-3}$. Fabrication of samples under the conditions indicated by the cross symbols was also attempted in this study. However, the samples could not be completely built because the recoater hit uneven surface of the samples and stopped. The uneven surfaces were due to too high laser energy (high laser output and slow scan speed). The higher laser energy causes molten metal to flow by the recoil pressure and Marangoni convection [27, 28]. As the metal solidifies while flowing, unevenness is generated on the surface of the fabricated sample.

In this study, the building direction was defined as the positive direction of the z-axis. The surfaces in perpendicular and horizontal to the building direction are denoted as the XY plane and XZ plane, respectively. To evaluate the relative density, melt pool depth, and microhardness (HV), the built bulk samples were cut out from the base plate. Then, the densities of the samples were measured using the Archimedes method. The built bulk samples were mechanically polished with emery papers and buffed with a 3 μm diamond slurry, followed by the final polishing with a colloidal silica. The samples' microhardness values were measured on the XY and XZ planes using a Vickers indenter (FUTURE-TECH CORP., FM-300e) at a constant load of 9.8 N at ambient temperature. The polished samples were etched with nital solution at room temperature. Finally, ten melt pools on the XZ plane near a top surface of each sample were observed with an optical microscope.

The maximum depths of each semicircular melt pool from the top surface was measured and averaged to obtain the melt pool depth.

In this study, the ratio of the deposited energy density (ΔH) to the enthalpy at melting (h_s), which is expressed by Eq. (2), was applied to summarize the results.

$$\frac{\Delta H}{h_s} = \frac{AP}{h_s \sqrt{\pi D v \sigma^3}}, \quad (2)$$

where A is the laser absorptivity, D is the thermal diffusivity, respectively. σ is the laser spot size (half-width of gaussian beam [29]), which is determined by the laser wavelength, the incident diameter to the optical system, the lens performance, and the focal length, and denoted as the optical spot size in this study. The deposited energy density (ΔH) has the same unit (Joule per unit volume) as the volumetric energy density. This parameter was originally proposed by Hann et al. [29] and used to investigate the correlation between the melt pool depth normalized by the spot size and the laser condition [30]. In Eq. (2), materials properties like A , D , and h_s are included. It is assumed that change in microstructure or properties (e.g., the relative density) can be always clarified based on only Eq. (2) even if different materials are applied. A , D , and h_s are constants in this study because only a maraging steel powder was used. In addition, the optical spot size (σ) is also a constant. Therefore, $P \cdot v^{-1/2}$ was used based on Eq. (2) to simplify the parameter by removing constants. Since the parameters other than P and v are constants in the present study, the main difference between volumetric and deposited energy densities is the power index of the scanning speed, which contributes to the volumetric energy density as v^{-1} and to the deposited energy density as $v^{-1/2}$.

3. Results

Figure 2(a, b) shows the typical optical microscopy images of the samples (XZ plane) fabricated under a (a) low laser condition (85 W and 2,500 mm s⁻¹) and (b) high laser condition (160 W and 1,250 mm s⁻¹), and (c) the change in the relative density as a function of the volumetric energy density. In Fig. 2(a), the dark contrast represents the pores. The relative density of this sample was approximately 74.8%, as shown in Fig. 2(c). Under low laser conditions (low laser power and high scan speed), the samples included many pores, and the morphology of the raw material powder was partially retained. Dense materials were obtained under high laser conditions (high laser power and low scan speed), as shown in Fig. 2(b). The relative density of this sample was approximately 99.8%. The relative density tended to increase as the volumetric energy density increased (Fig. 2(c)). However, the relative density had considerable variation even under conditions with

approximately the same volumetric energy density. For example, when the volumetric energy density was $68 \text{ J} \cdot \text{mm}^{-3}$, the maximum relative density was 99.4% (dense) and the minimum density was 78.0% (porous). Therefore, the volumetric energy density cannot be always used as a measure to obtain the conditions necessary to fabricate dense materials.

Figure 3(a, b) shows the optical microscopy images of the samples (XY plane) under (a) 170 W and $2,500 \text{ mm s}^{-1}$ and (b) 230 W and $1,667 \text{ mm s}^{-1}$, and (c) the change in the melt pool depth as a function of the volumetric energy density. The data points and error bars indicate the average value and standard deviation of the measured depths of ten melt pools. Note that the number of data points shown in Fig. 3(c) is smaller than the number of samples. This is because many pores existed in samples with low relative density, and thus the melt pools could not be clearly distinguished. The melt pool depth changed depending on the laser condition, and a higher laser condition generated a deeper melt pool. The samples shown in Fig. 3(a, b) had a melt pool depth of approximately $60 \text{ }\mu\text{m}$ and approximately $130 \text{ }\mu\text{m}$, respectively, as shown in Fig. 3(c). Keyholes, which often arise due to exceeding the boiling temperature of the material under extremely high laser conditions, were not observed [30, 31]. As shown in Fig. 3(c), the melt pool depth tended to increase as the volumetric energy density increased. However, the melt pool depth differed largely, even when the volumetric energy density had almost the same value. When the data points regressed linearly, the correlation coefficient was $R=0.686$. When the volumetric energy density was 68 J mm^{-3} , the maximum melt pool depth was approximately $100 \text{ }\mu\text{m}$ and approximately three times deeper than the bedded powder layer thickness ($30 \text{ }\mu\text{m}$). Additionally, the minimum melt pool depth was approximately $60 \text{ }\mu\text{m}$ and approximately twice deeper than $30 \text{ }\mu\text{m}$. This indicates that the melting times per one bedded-powder layer changed (two or three times). The melt pool was a trace of the heat input into the material. The fact that the melt pool depth cannot be understood by the volumetric energy density suggests that the assumed thermal distribution is not valid.

Figure 4 shows the change in the Vickers hardness as a function of (a) the volumetric energy density and (b) the relative density. The open and closed symbols indicate the hardness measured at the XY and XZ plane, respectively. The data points and error bars indicate the average value and standard deviation of the Vickers hardness measured at the five portions. The Vickers hardness tended to increase as the volumetric energy density increased. However, the Vickers hardness varied drastically, particularly when the volumetric energy density was $68 \text{ J} \cdot \text{mm}^{-3}$. As shown in Fig. 4 (b), the Vickers hardness increased as the relative density increased. The dominant factor of the change in the Vickers hardness was the number of pores. Under low laser conditions, the samples

include many pores, which results in the decrease of the Vickers hardness. It is noted that the Vickers hardness cannot be clarified by the volumetric energy density because the relative density cannot be understood (Fig. 2(c)). The Vickers hardness of the dense materials (plotted near the relative density of 100%) was approximately 400 HV, which is in good agreement with previous reports [11, 12]. This hardness value was higher than that of the solution heat-treated maraging steel fabricated using conventional processes (approximately 300 HV) [32, 33]. Moreover, the Vickers hardness did not differ much regardless of the measurement surface (XY plane and XZ plane).

Figure 5 indicates the correlation between the relative density and $P \cdot v^{-1/2}$ (deposited energy density). The change in the relative density could be approximated by a single curve. The relative density increased when $P \cdot v^{-1/2}$ was less than approximately $3.3 \text{ W} \cdot \text{mm}^{-1/2} \cdot \text{s}^{1/2}$, and became almost constant at approximately 100% (dense) when $P \cdot v^{-1/2}$ exceeded the value. Although there is some variation in the relative density even in the dense region, the deposited energy density can roughly provide the threshold laser condition from porous to dense. This result means that the laser conditions for fabricating dense materials can be designed by $P \cdot v^{-1/2}$ instead of the volumetric energy density. Note that the threshold value depends on the other laser parameters such as the spot size, hatch-spacing between adjacent laser-scanning tracks, bedded-powder layer thickness, and so on.

Figure 6 shows the change in the melt pool depth as a function of $P \cdot v^{-1/2}$ based on the deposited energy density. The variation became smaller in comparison with the variation shown in Fig. 3 (c). In fact, when the data points regressed linearly, the correlation coefficient (R) was $R=0.934$, which is better than the correlation coefficient between the melt pool depth and volumetric energy density ($R=0.686$). Additionally, the melt pool depth increased almost linearly as $P \cdot v^{-1/2}$ increased. This result suggests that the thermal distribution assumed in the deposited energy density is valid. The melt pool depth was approximately $70 \mu\text{m}$ when $P \cdot v^{-1/2}$ was approximately $3.3 \text{ W} \cdot \text{mm}^{-1/2} \cdot \text{s}^{1/2}$. Assuming that the regression line can be extrapolated to the low $P \cdot v^{-1/2}$ region, the melt pool depth was smaller than approximately $60 \mu\text{m}$ in the case of low relative density. Thus, it was found that a bedded-powder layer must melt more than twice to make the materials dense.

Figure 7 presents the change in the Vickers hardness as a function of $P \cdot v^{-1/2}$. The change in the Vickers hardness can be approximated by one curve such as the relative density. The Vickers hardness increased when $P \cdot v^{-1/2}$ was less than approximately $3.3 \text{ W} \cdot \text{mm}^{-1/2} \cdot \text{s}^{1/2}$, and became almost constant at approximately 400 HV when $P \cdot v^{-1/2}$ exceeded the value. Again, it was confirmed that $P \cdot v^{-1/2}$ (deposited energy density) was an effective choice as the laser condition to fabricate satisfactory materials.

4. Discussion

In this study, the effects of the laser power and scan speed on the relative density, melt pool depth, and Vickers hardness of the selectively laser melted maraging steel were investigated. The changes in the relative density, melt pool depth, and Vickers hardness were not always clarified by using the volumetric energy density (Figs. 2-4), which is widely used in the SLM process. On the other hand, using the deposited energy density enabled the expression of the changes in these parameters by a single curve (Figs. 5-7), owing to the difference in the models assumed in each energy density, as shown in Fig. 8. Both the volumetric and deposited energy densities had the same unit (Joule per unit volume) but were normalized by different volume. In the volumetric energy density model shown in Fig. 8 (a), the heat-distributed region per unit time is a rectangular parallelepiped with a size of $v \times S \times t$. The laser energy per unit time is P , and Eq. (1) is obtained by dividing P by $v \times S \times t$. This model assumes that heat is always transferred in a depth of the bedded-powder thickness (t) even when the scan speed (v) changes. However, this is not reasonable because different v changes the time during which laser is irradiated to a certain point, and the depth in which heat is transferred during the time. On the other hand, in the deposited energy density model shown in Fig. 8(b), the heat-distributed region is a cylinder with a volume of $\pi\sigma^2(D\tau)^{1/2}$ [30], where τ is the dwell time, during which the laser is irradiated to a certain point. The laser heat irradiated during τ is $P\tau$, and the heat absorbed in the material is $AP\tau$. Eq. (2) is obtained by dividing $AP\tau$ by $\pi\sigma^2(D\tau)^{1/2}$ although numerical coefficient is different because Hann et al. have taken thermal distribution into stricter consideration [29]. Here, it is noted that the thermal diffusion length ($(D\tau)^{1/2}$) is used as a heat-distributed depth. $(D\tau)^{1/2}$ physically indicates the depth into which heat is transferred during the laser-irradiation and varies depending on the scan speed since τ is approximated by σ/v . The model of the deposited energy density is more appropriate than the model of the volumetric energy density. Consequently, the change in the relative density, melt pool depth, and Vickers hardness were clarified by using $P \cdot v^{-1/2}$ based on the deposited energy density.

The main difference between the volumetric and deposited energy densities is the power index of the scan speed, which contributes to the volumetric energy density as v^{-1} , but to the deposited energy density as $v^{-1/2}$. In the volumetric energy density, the contribution of the scan speed is the same as that of the laser power. For example, when both the laser output and scanning speed are doubled, the energy density does not change. However, the contribution of the scanning speed is actually smaller than the contribution of laser power. When the laser power doubled, equal deposited energy density, which

provides an approximately equal relative density, is obtained by quadrupling the scan speed. In other words, if the laser power is increased slightly, the building speed will increase largely. The deposited energy density offers important insights with regard to productivity improvement pertaining to the processes of additive manufacturing.

The deposited energy density has been used to clarify the correlation between the melt pool depth normalized by the spot size and the laser condition, particularly in research fields related to welding. The results obtained by previous studies have revealed that the change in the normalized melt pool depth can be expressed by one curve as a function of the deposited energy density [29, 30]. The deposited energy density also provides the laser conditions under which the materials change from dense to porous, owing to the formation of the keyhole. The present study revealed that the relative density and Vickers hardness can be expressed by one curve as a function of the deposited energy density. The deposited energy density also provides the threshold laser condition ($P \cdot v^{-1/2} = \sim 3.3 \text{ W} \cdot \text{mm}^{-1/2} \cdot \text{s}^{1/2}$) from porous to dense. Thus, the deposited energy density provides both the upper and lower limits of the laser conditions to obtain dense materials. It is noted that the relative density is not always good (e.g., relative density <99%) in the dense region in Fig. 5. This is because only the thermal diffusion is considered in Eq. (2). As reported in the previous studies, the recoil pressure, Marangoni convection, and generation of sputter affects the relative density of the SLM-fabricated materials [27, 28]. By taking these effects into consideration, it is possible to estimate the laser conditions for obtaining high relative density more accurately.

The volumetric energy density has been widely used in research fields about the additive manufacturing processes. Some studies reported that the change in the relative density can be understood by the volumetric energy density [12, 24]. Figure 9 indicates the change in the relative density as functions of (a) the volumetric energy density, (b) $P \cdot v^{-1/2} \cdot \sigma^{3/2}$ based on the deposited energy density. In Fig. 9, the data reported in previous literatures [12, 24] were also shown. As indicated by the reference data shown in Fig. 10(a), the change in the relative density can be expressed by one curve using the volumetric energy density, which is different from this study. This is attributed to the difference in the range of laser conditions. In previous studies, the laser power and scan speed were in the range of 57-100 W and 100-600 mm s^{-1} , respectively. These ranges are narrower than the ranges used in this study (43-255 W and 417-3,000 mm s^{-1}). Consequently, the volumetric energy density seems to have been able to express the change of the relative density. However, the volumetric energy density is inappropriate for a wider range of laser conditions such as those used in this study. In Fig. 9 (b), $P \cdot v^{-1/2} \cdot \sigma^{3/2}$ is used instead of $P \cdot v^{-1/2}$ because the spot sizes in the previous studies were

different to those used in this study. The change in the relative density could not be clarified by $P \cdot v^{-1/2} \cdot \sigma^{-3/2}$. For example, the relative density reported by Casalino et al. [24] reached approximately 100% at the smallest $P \cdot v^{-1/2} \cdot \sigma^{-3/2}$. This is due to the difference in the hatch-spacing between the adjacent laser-scanning track (S) and the bedded powder thickness (t). In previous reports, these parameters were different to the parameters used in this study. Additionally, these parameters are not included in Eq. (2) because the equation of the deposited energy density does not assume that the laser is irradiated multiple times, in the same way as in SLM, but rather that the laser scanned once in one direction. Thus, the effect of the SLM process parameters cannot be completely clarified by Eq. (2), which must be modified further to express the effects of the process parameters comprehensively. Especially when the hatch distance changes, it is necessary to consider the effects of not only the optical spot size in Eq. (2) but also effective spot size (powder melting region). In other words, it is expected that the relative density changes depending on how much region where powder is actually melted is overlapped. Moreover, various existing studies have reported that the microstructure in SLM-fabricated materials can be controlled by laser-scanning strategies [34, 35]. Therefore, it is necessary to investigate whether the microstructure can be controlled based on the deposited energy density.

5. Conclusions

The effects of the laser power and the scan speed on the relative density, melt pool depth, and the Vickers hardness of the SLM-fabricated maraging steel were investigated. The relative density, melt pool depth, and Vickers hardness exhibited large variation even when the volumetric energy density had the same value. It is concluded that the change in these structural factors and the hardness cannot be always clarified by the volumetric energy density, which is widely used in research fields related to the SLM process. Moreover, $P \cdot v^{-1/2}$ based on the deposited energy density enables the change in these values to be represented by one curve and provides a threshold value for the laser conditions to fabricate dense materials. This is caused by the difference in the thermal distribution model. Considering the thermal diffusion length, the deposited energy density is more physically reasonable than the volumetric energy density. Although the deposited energy density provides the upper and lower limits of the laser condition to fabricate dense materials, it must be modified to express the effect of other process parameters.

Acknowledgments

This work was supported by “Knowledge Hub Aichi,” which is a Priority Research Project of the Aichi Prefectural Government, Japan. We are grateful for the technical

support provided by Dr. Y. Ishida in the preparation of the samples.

References

1. L. E. Murr, S. M. Gaytan, D. A. Ramirez, E. Martinez, J. Hernandez, K. N. Amato, P. W. Shindo, F. R. Medina, R. B. Wicker, Metal Fabrication by Additive Manufacturing Using Laser and Electron Beam Melting Technologies, *J. Mater. Sci. Technol.* 28 (2012) 1–14.
2. W. E. King, A. T. Anderson, R. M. Ferencz, N. E. Hodge, C. Kamath, S. A. Khairallah, A. M. Rubenchi, Laser powder bed fusion additive manufacturing of metals: physics, computational, and materials challenges, *App. Phys. Rev.* 2 (2015) 041304.
3. W. J. Sames, F. A. List, S. Pannala, R. R. Dehoff, S. S. Babu, The metallurgy and processing science of metal additive manufacturing, *Int. Mater. Rev.* 61 (2016) 1–46.
4. D. Herzog, V. Seyda, E. Wycisk, C. Emmelmann, Additive manufacturing of metals, *Acta Mater.* 117 (2016) 371–392.
5. M. Tang, P. C. Pistorius, S. Narra, J. L. Beuth, Rapid Solidification: Selective Laser Melting of AlSi10Mg, *JOM* 68 (2016) 960–966.
6. X. Ding, L. Wang, Heat transfer and fluid flow of molten pool during selective laser melting of AlSi10Mg powder: Simulation and experiment, *J. Manuf. Proc.* 26 (2017) 280–289.
7. N. Takata, H. Kodaira, K. Sekizawa, A. Suzuki, M. Kobashi, Microstructure and mechanical properties of Al–10Si–0.4Mg alloy fabricated by selective laser melting, *J. Jpn Inst. Light Metals*, 67(11) (2017) 582–588.
8. L. Thijs, K. Kempen, J. P. Kruth, J. V. Humbeeck, Fine-structured aluminium products with controllable texture by selective laser melting of pre-alloyed AlSi10Mg powder, *Acta Materialia* 61 (2013) 1809–1819.
9. P. Kumar, O. Prakash, U. Ramamurty, Micro-and meso-structures and their influence on mechanical properties of selectively laser melted Ti-6Al-4V, *Acta Materialia* 154 (2018) 246-260.
10. K. N. Amato, S. M. Gaytan, L. E. Murr, E. Martinez, P. W. Shindo, J. Hernandez, S. Collins, F. Medina, Microstructures and mechanical behavior of Inconel 718 fabricated by selective laser melting, *Acta Materialia* 60 (2012) 2229–2239.
11. R. Casati, J. N. Lemke, A. Tuissi, M. Vedani, Aging Behaviour and Mechanical Performance of 18-Ni 300 Steel Processed by Selective Laser Melting, *Metals* 6 (2016) 218.
12. K. Kempen, E. Yasa, L. Thijs, J. P. Kruth, J. V. Humbeeck, Microstructure and mechanical properties of Selective Laser Melted 18Ni-300 steel, *Phys. Procedia* 12

(2011) 255–263.

13. C. Tan, K. Zhou, W. Ma, P. Zhang, M. Liu, T. Kuang, Microstructural evolution, nanoprecipitation behavior and mechanical properties of selective laser melted high-performance grade 300 maraging steel, *Mater. Des.* 134 (2017) 23–34.
14. W. Du, Q. Bai, B. Zhang, A Novel Method for Additive/Subtractive Hybrid Manufacturing of Metallic Parts, *Procedia Manufacturing* 5 (2016) 1018–1030.
15. ASM International. *ASM Handbook Volume 2: Properties and Selection: Nonferrous Alloys and Special Purpose Materials*, ASM International: Materials Park, OH, USA, 1990.
16. G. Meneghetti, D. Rigon, D. Cozzi, W. Waldhauser, M. Dabalà, Influence of building orientation on static and axial fatigue properties of maraging steel specimens produced by additive manufacturing, *Struct. Integr. Procedia* 7 (2016) 149–157.
17. R. Branco, J. D. M. Costa, F. Berto, S. M. J. Razavi, J. A. M. Ferreira, C. Capela, L. Santos, F. Antunes, Low-Cycle Fatigue Behaviour of AISI 18Ni300 Maraging Steel Produced by Selective Laser Melting, *Metals* 8 (2018) 32.
18. J. Tian, Z. Huang, W. Qi, Y. Li, J. Liu, G. Hu, Dependence of Microstructure, relative density and hardness of 18Ni-300 maraging steel fabricated by selective laser melting on the energy density, In *CMC2017: Advances in Materials Processing*; Springer: Singapore, (2018) 229–241.
19. N. Takata, R. Nishida, A. Suzuki, M. Kobashi, M. Kato, Crystallographic Features of Microstructure in Maraging Steel Fabricated by Selective Laser Melting, *Metals* 8 (2018) 440.
20. T. Kimura, T. Nakamoto, Thermal and mechanical properties of commercial-purity aluminum, *J. Jpn Inst. Light Metals*, 66(4) (2016) 167–173.
21. E. Liverani, S. Toschi, L. Ceschini, A. Fortunato, Effect of selective laser melting (SLM) process parameters on microstructure and mechanical properties of 316L austenitic stainless steel fabricated using selective laser melting, *Journal of Materials Processing Tech.* 249 (2017) 255–263.
22. H. Gong, K. Rafia, H. Gao, T. Starra, B. Stuckera, Analysis of defect generation in Ti–6Al–4V parts made using powder bed fusion additive manufacturing processes, *Additive Manufacturing* 1–4 (2014) 87–98.
23. Y. Bai, Y. Yang, D. Wang, M. Zhang, Influence mechanism of parameters process and mechanical properties evolution mechanism of maraging steel 300 by selective laser melting, *Materials Science & Engineering A* 703 (2017) 116–123.
24. G. Casalino, S. L. Campanelli, N. Contuzzi, A. D. Ludovico, Experimental investigation and statistical optimisation of the selective laser melting process of a

- maraging steel, *Optics & Laser Technology* 65 (2015) 151–158.
25. U. S. Bertoli, A. J. Wolfer, M. J. Matthews, J. P. R. Delplanque, J. M. Schoenung, On the limitations of Volumetric Energy Density as a design parameter for Selective Laser Melting, *Materials and Design* 113 (2017) 331–340.
 26. J. Metelkova, Y. Kinds, K. Kempen, C. de Formanoir, A. Witvrouw, B. Van Hooreweder, On the influence of laser defocusing in Selective Laser Melting of 316L, *Additive Manufacturing*, 23 (2018) 161–169.
 27. C. Qiu, C. Panwisawas, M. Ward, H. C. Basoalto, J. W. Brooks, M. M. Attallah, On the role of melt flow into the surface structure and porosity development during selective laser melting, *Acta Mater.* 96 (2015) 72–79.
 28. S. A. Khairallah, A. T. Anderson, A. Rubenchik, W. E. King, Laser powder-bed fusion additive manufacturing: Physics of complex melt flow and formation mechanisms of pores, spatter, and denudation zones, *Acta Mater.* 108 (2016) 36–45.
 29. D. B. Hann, J. Iammi, J. Folkes, A simple methodology for predicting laser-weld properties from material and laser parameters, *J. Phys. D: Appl. Phys.* 44 (2011) 445401.
 30. W. E. King, H. D. Barth, V. M. Castillo, G. F. Gallegos, J. W. Gibbs, D. E. Hahn, C. Kamath, A. M. Rubenchik, Observation of keyhole-mode laser melting in laser powder-bed fusion additive manufacturing, *Journal of Materials Processing Technology* 214 (2014) 2915–2925.
 31. M. Araki, S. Kusakawa, K. Nakamura, M. Yonehara, T. Ikeshoji, H. Kyogoku, Parameter Optimization on the Fabrication of Al-10Si-0.4Mg Alloy Using Selective Laser Melting Process, *J. Jpn. Soc. Powder Powder Metallurgy*, 65(7) (2018) 383–388.
 32. E.A. Jäggle, Z. Sheng, P. Kürnsteiner, S. Ocylok, A. Weisheit, D. Raabe, Comparison of Maraging Steel Micro- and Nanostructure Produced Conventionally and by Laser Additive Manufacturing, *Materials* 10 (2017) 8.
 33. J. M. Pardal, S. S. M. Tavares, V. F. Terra, M. R. Da Silva, D. R. Dos Santos, Modeling of precipitation hardening during the aging and overaging of 18Ni–Co–Mo–Ti maraging 300 steel, *J. Alloys Compd.* 393 (2005) 109–113.
 34. A. Reza, A. Dezfoli, W. S. Hwang, W. C. Huang, T. W. Tsai, Determination and controlling of grain structure of metals after laser incidence: Theoretical approach, *Scientific Reports* 7 (2017) 41527.
 35. S. H. Sun, K. Hagihara, T. Nakano, Effect of scanning strategy on texture formation in Ni-25 at.%Mo alloys fabricated by selective laser melting, *Materials and Design* 140 (2018) 307–316.

Captions

- Fig. 1. (a) Appearance of 25 cubic samples fabricated under different laser conditions and (b) laser conditions applied in this study. The circles close to the numbers correspond to the building condition of samples in (a), and the crosses correspond to the conditions under which samples could not be built.
- Fig. 2. (a, b) Optical microscopy images of samples fabricated under (a) 85 W and 2,500 mm s⁻¹ and (b) 160 W and 1,250 mm s⁻¹; (c) change in relative density as a function of volumetric energy density.
- Fig. 3. (a, b) Optical microscopy images under (a) 170 W and 2,500 mm s⁻¹ and (b) 230 W and 1,667 mm s⁻¹; (c) change in melt pool depth as a function of volumetric energy density.
- Fig. 4. Change in Vickers hardness as functions of (a) the volumetric energy density and (b) relative density.
- Fig. 5. Change in relative density as a function of $P \cdot v^{-1/2}$ based on deposited energy density.
- Fig. 6. Change in melt pool depth as a function of $P \cdot v^{-1/2}$ based on deposited energy density.
- Fig. 7. Change in Vickers hardness as a function of $P \cdot v^{-1/2}$ based on deposited energy density.
- Fig. 8. Schematic illustrations of models assumed in (a) the volumetric energy density and (b) deposited energy density.
- Fig. 9. Change in relative density as functions of (a) the volumetric energy density and (b) $P \cdot v^{-1/2} \cdot s^{-3/2}$ based on the deposited energy density.

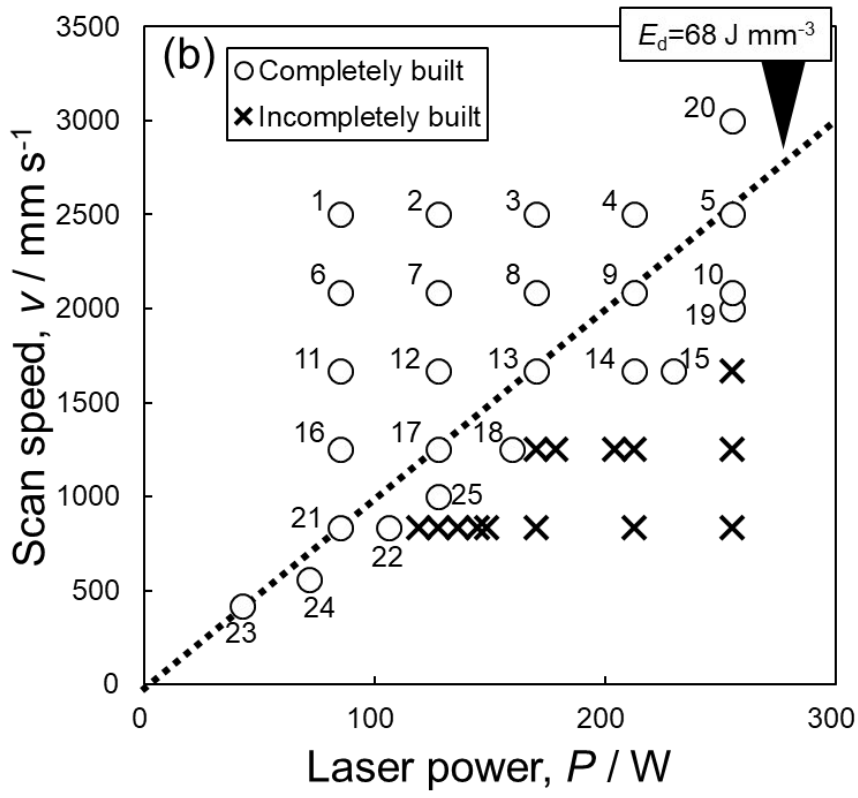
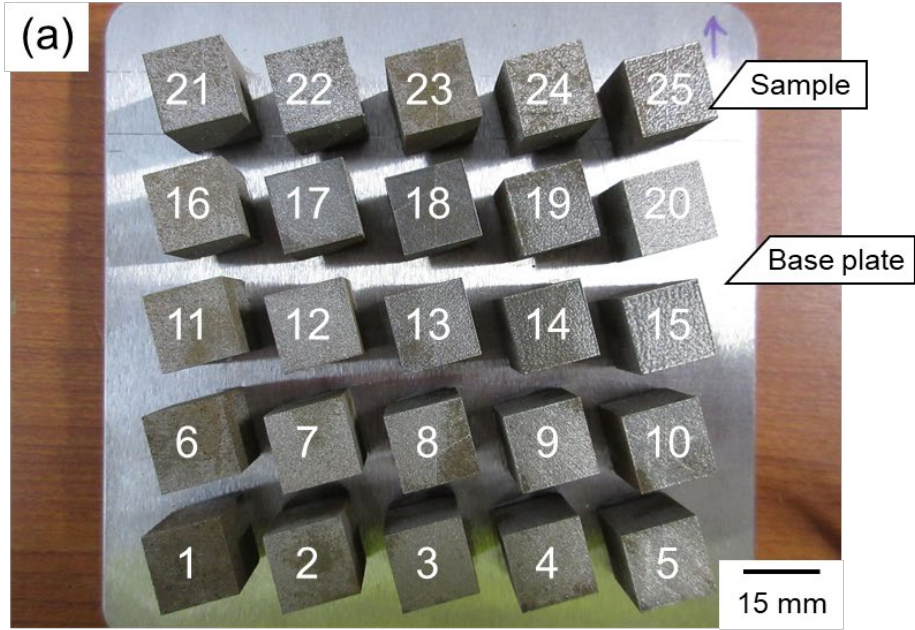


Fig. 1.

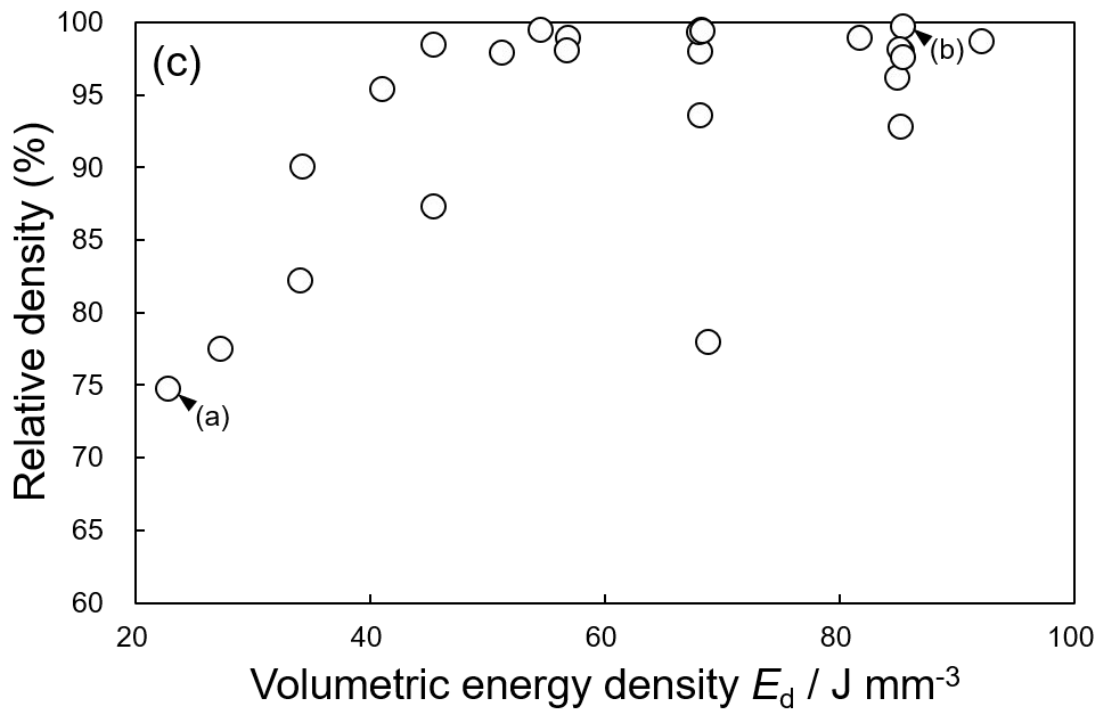
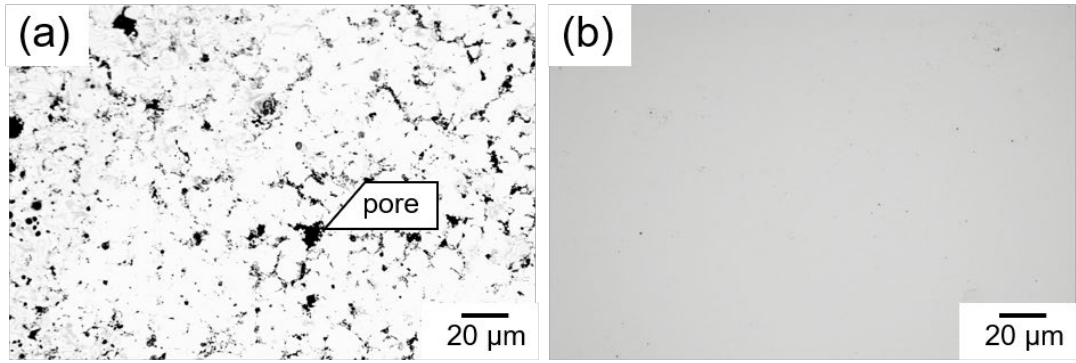


Fig. 2.

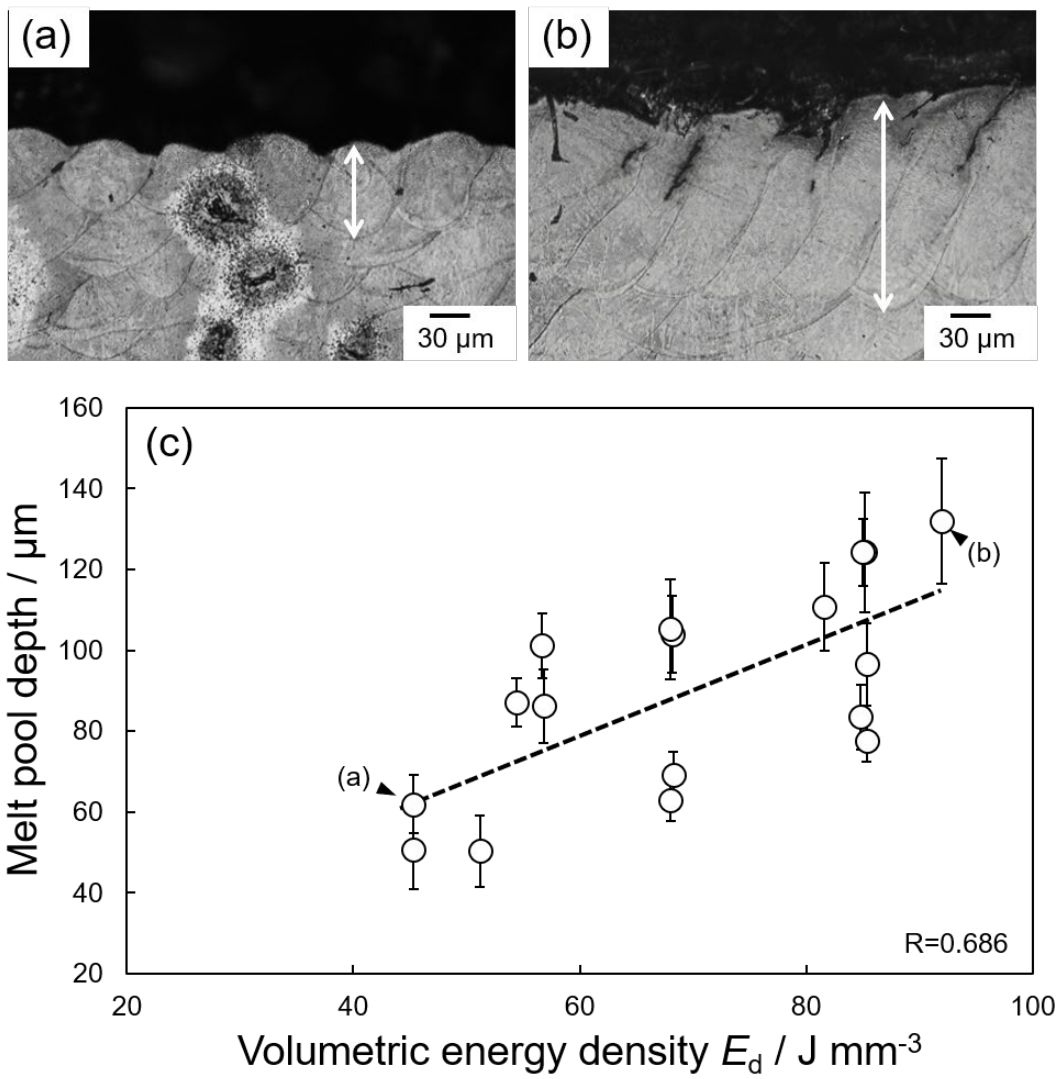


Fig. 3.

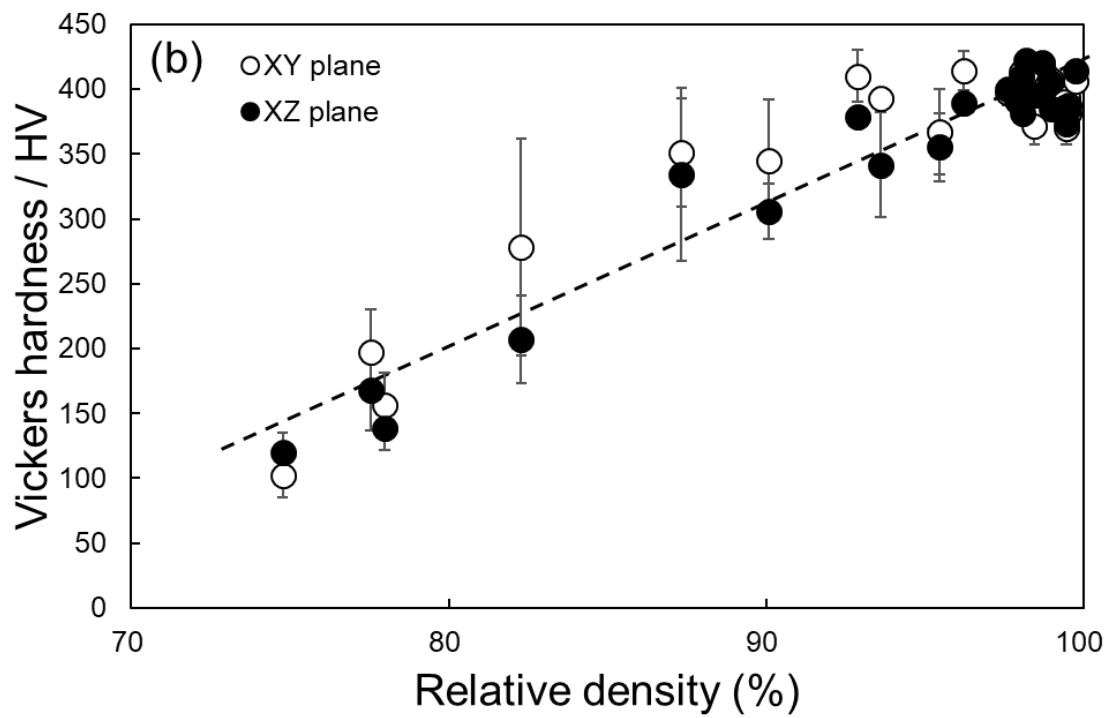
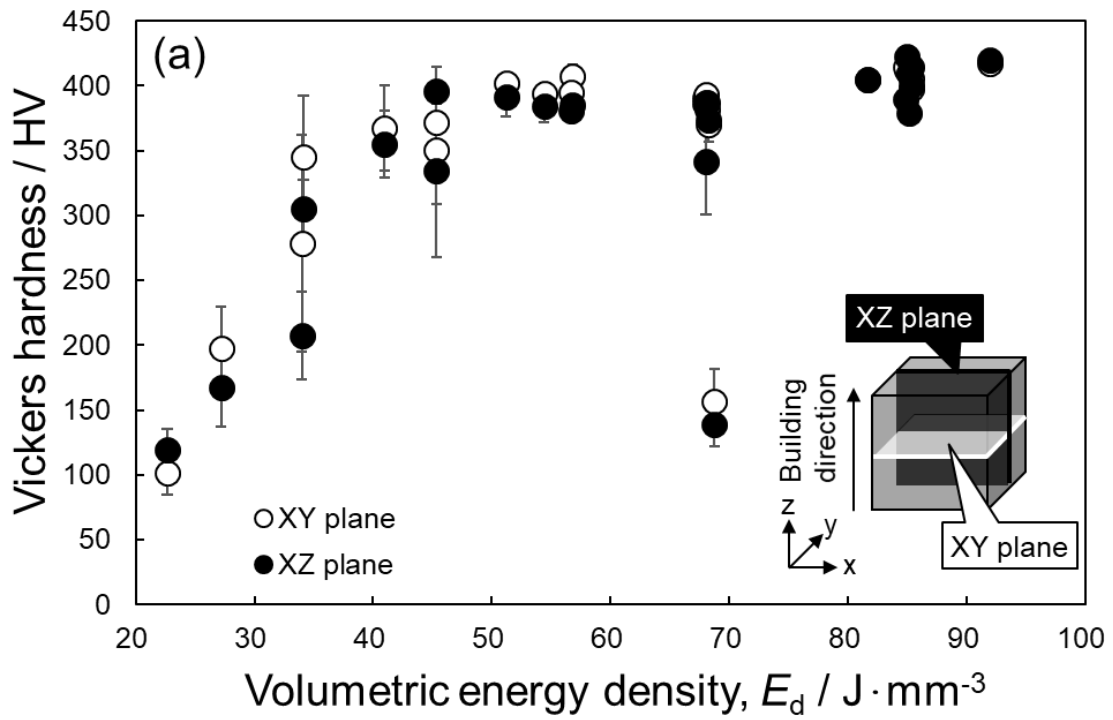


Fig. 4.

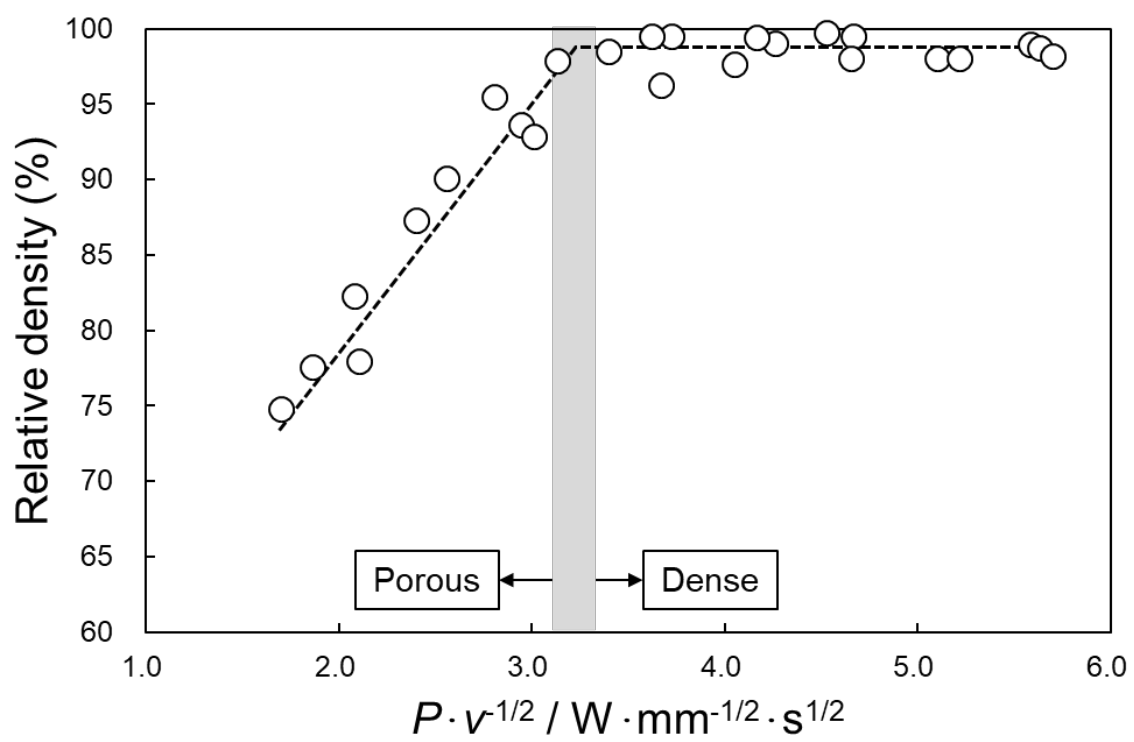


Fig. 5.

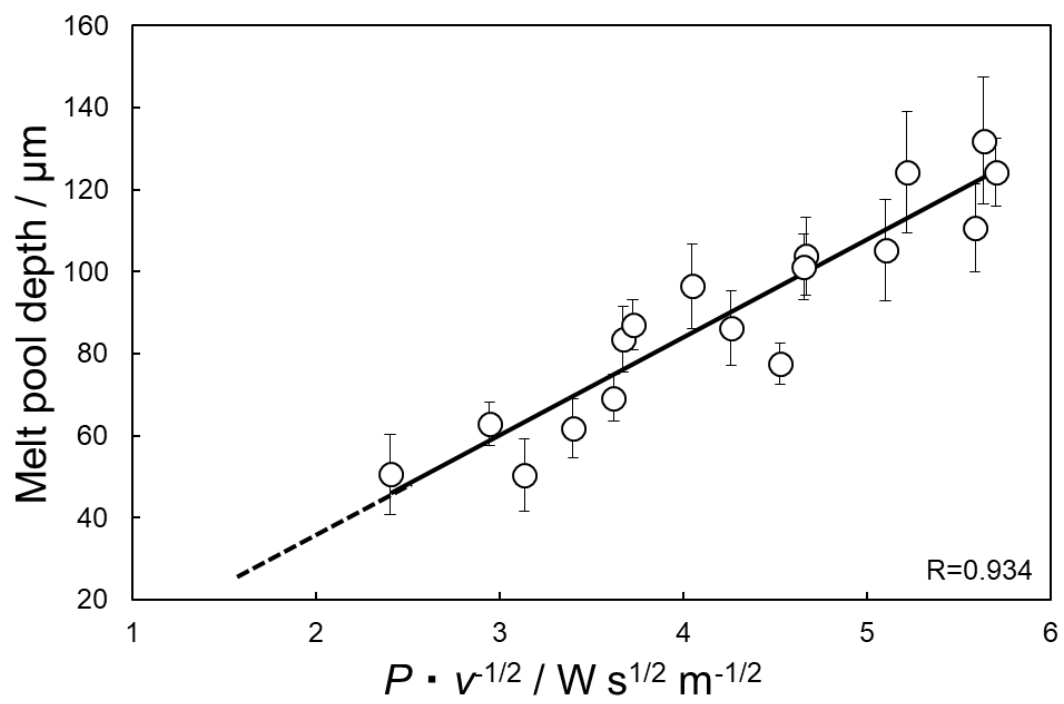


Fig. 6.

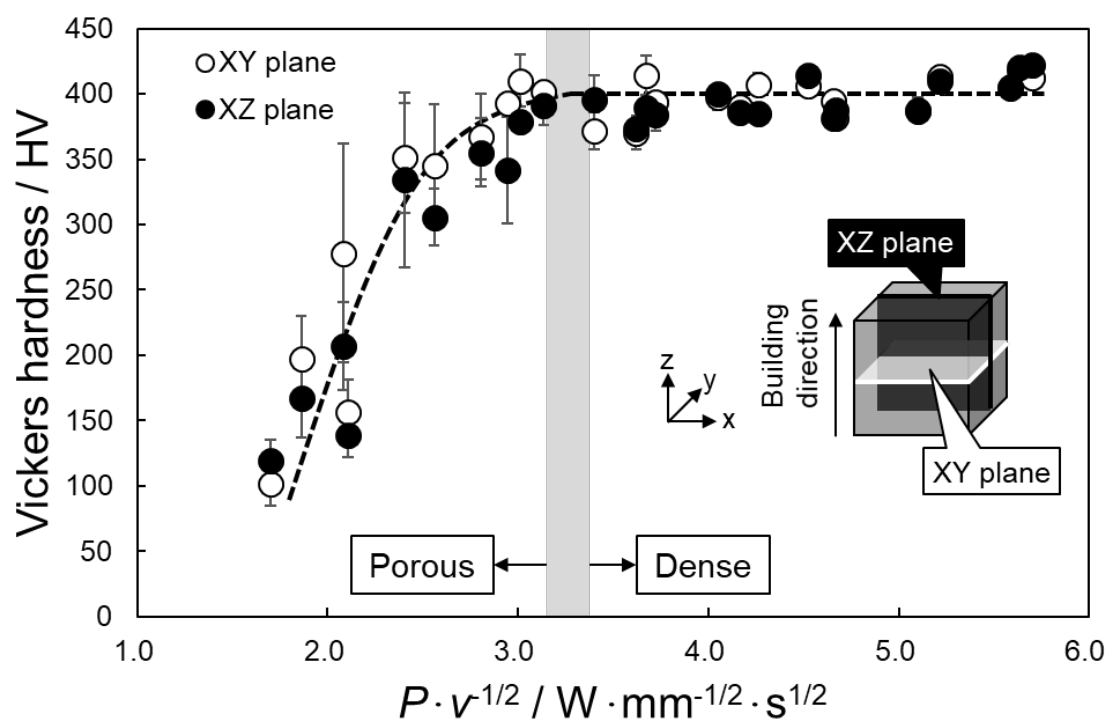
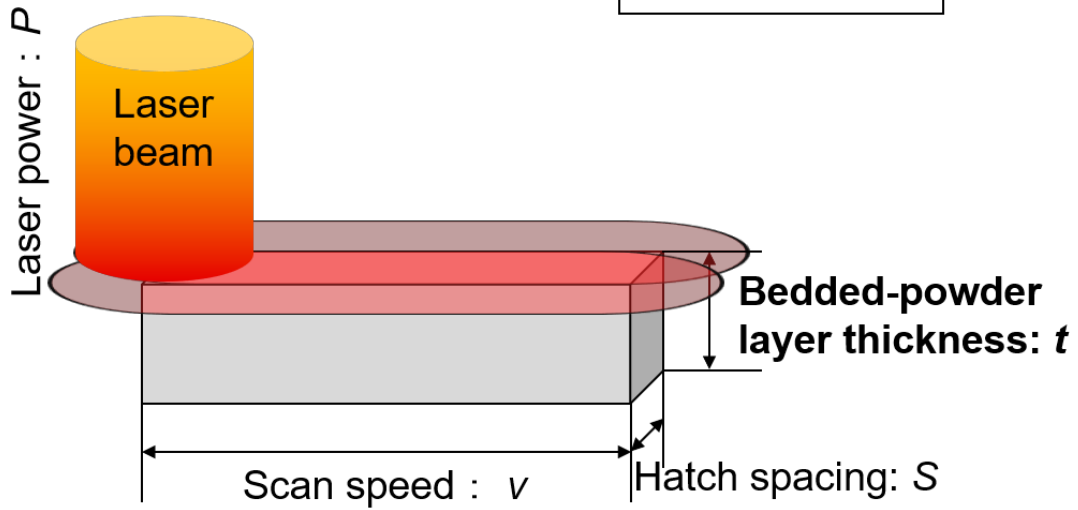


Fig. 7.

(a) Volumetric energy density

$$E_d = \frac{P}{v \cdot S \cdot t}$$



(b) Deposited energy density

$$\Delta H = \frac{AP}{\sqrt{\pi D v \sigma^3}}$$

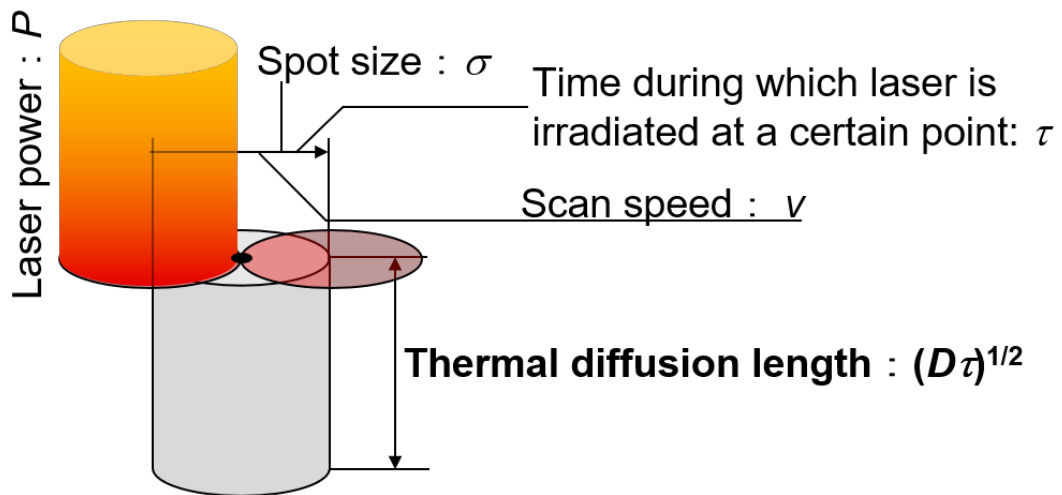


Fig. 8.

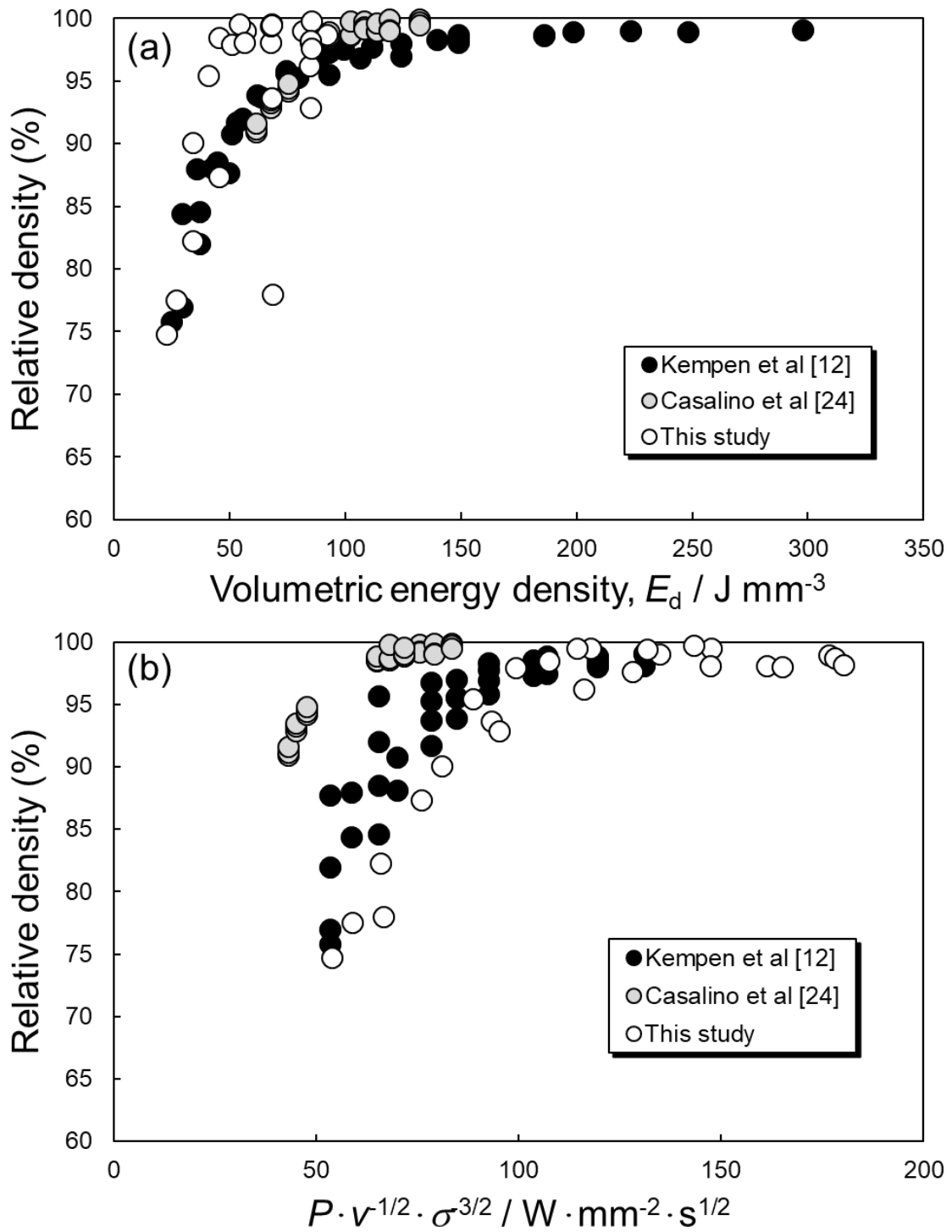


Fig. 9.